Evaluation of (*rac*)-, (*R*)-, and (*S*)-^{18}F-OF-NB1 for Imaging GluN2B Subunit–Containing *N*-Methyl-D-Aspartate Receptors in Nonhuman Primates

Hazem Ahmed*[1,2], Ming-Qiang Zheng*[2], Kelly Smart[2], Hanyi Fang[2,3], Li Zhang[2], Paul R. Emery[2], Hong Gao[2], Jim Ropchan[2], Ahmed Haider[1], Gilles Tamagnan[2], Richard E. Carson[2], Simon M. Ametamey[1], and Yiyun Huang[2]

[1]*Institute of Pharmaceutical Sciences, ETH Zurich, Zurich, Switzerland;* [2]*PET Center, Yale University, New Haven, Connecticut; and* [3]*Union Hospital, Huazhong University of Science and Technology, Wuhan, China*

Despite 2 decades of research, no *N*-methyl-D-aspartate (NMDA) glutamate receptor (GluN) subtype 2B (GluN1/2B) radioligand is yet clinically validated. Previously, we reported on (*rac*)-^{18}F-OF-NB1 as a promising GluN1/2B PET probe in rodents and its successful application for the visualization of GluN2B-containing NMDA receptors in postmortem brain tissues of patients with amyotrophic lateral sclerosis. In the current work, we report on the *in vivo* characterization of (*rac*)-, (*R*)-, and (*S*)-^{18}F-OF-NB1 in nonhuman primates. **Methods:** PET scans were performed on rhesus monkeys. Plasma profiling was used to obtain the arterial input function. Regional brain time–activity curves were generated and fitted with the 1- and 2-tissue-compartment models and the multilinear analysis 1 method, and the corresponding regional volumes of distribution were calculated. Blocking studies with the GluN1/2B ligand Co 101244 (0.25 mg/kg) were performed for the enantiopure radiotracers. Receptor occupancy, nonspecific volume of distribution, and regional binding potential (BP_{ND}) were obtained. Potential off-target binding toward σ_1 receptors was assessed for (*S*)-^{18}F-OF-NB1 using the σ_1 receptor ligand FTC-146. **Results:** Free plasma fraction was moderate, ranging from 12% to 16%. All radiotracers showed high and heterogeneous brain uptake, with the highest levels in the cortex. (*R*)-^{18}F-OF-NB1 showed the highest uptake and slowest washout kinetics of all tracers. The 1-tissue-compartment model and multilinear analysis 1 method fitted the regional time–activity curves well for all tracers and produced reliable regional volumes of distribution, which were higher for (*R*)- than (*S*)-^{18}F-OF-NB1. Receptor occupancy by Co 101244 was 85% and 96% for (*S*)-^{18}F-OF-NB1 and (*R*)-^{18}F-OF-NB1, respectively. Pretreatment with FTC-146 at both a low (0.027 mg/kg) and high (0.125 mg/kg) dose led to a similar reduction (48% and 49%, respectively) in specific binding of (*S*)-^{18}F-OF-NB1. Further, pretreatment with both Co 101244 and FTC-146 did not result in a further reduction in specific binding compared with Co 101244 alone in the same monkey (82% vs. 81%, respectively). Regional BP_{ND} values ranged from 1.3 in the semiovale to 3.4 in the cingulate cortex for (*S*)-^{18}F-OF-NB1. **Conclusion:** Both (*R*)- and (*S*)-^{18}F-OF-NB1 exhibited high binding specificity to GluN2B subunit–containing NMDA receptors. The fast washout kinetics, good regional BP_{ND} values, and high plasma free fraction render (*S*)-^{18}F-OF-NB1 an attractive radiotracer for clinical translation.

Key Words: NMDA; GluN2B subunit; brain PET imaging; nonhuman primates; neurodegeneration

Received Feb. 7, 2022; revision accepted Apr. 7, 2022.

For correspondence or reprints, contact Yiyun Henry Huang (henry.huang@yale.edu) or Simon M. Ametamey (simon.ametamey@pharma.ethz.ch).

*Contributed equally to this work.

Published online Jun. 16, 2022.

J Nucl Med 2022; 63:1912–1918
DOI: 10.2967/jnumed.122.263977

Glutamatergic *N*-methyl-D-aspartate receptors (NMDARs) are heterotetrameric ion channels ubiquitously expressed in the mammalian brain. The receptor complex is assembled from distinct subunits, namely *N*-methyl-D-aspartate (NMDA) glutamate receptor (GluN) subtypes 1a–1h (GluN1(a–h)), GluN subtypes 2A–2D (GluN2(A–D)), and GluN subtypes 3A and 3B, where each GluN2 subtype exhibits a unique spatiotemporal expression and function (*1*). NMDARs are known to be the linchpin for synaptic plasticity and transmission as well as higher cognitive functions. Notably, synaptic NMDARs are promotors of cell survival whereas extrasynaptic GluN2B subunit–enriched NMDARs are mediators of cell death. The GluN1/2B receptors are associated with several neuropathologies, such as Alzheimer's disease, Parkinson's disease, depression, schizophrenia, and stroke, among others (*2–5*). As such, the development of GluN1/2B antagonists has been the prime focus of therapeutic development efforts over the past 2 decades, with 19 therapeutic patent applications published in the past 5 years alone (*6,7*). Although these subtype-selective antagonists possess pharmacologic action similar to conventional NMDA ion channel blockers, they exhibit a much more favorable neurologic safety profile, as their selectivity is thought to preserve the physiologic functions of NMDARs but minimize potential undesired pharmacologic effects (*4,8*). To date, several GluN1/2B antagonists, such as CERC-301, have been evaluated in clinical trials with no-to-modest clinical benefits, whereas others are still in development (*7,9*). PET imaging is a powerful modality that can accelerate drug development—for example, to be used in target engagement and drug occupancy studies—and serve as a credible tool in patient selection and monitoring (*10,11*). Despite the long-standing interest, efforts to develop a GluN1/2B-specific PET radioligand have largely been unsuccessful. Challenges include poor brain uptake, homogeneous distribution, and the existence of brain radiometabolites, as well as binding to other brain receptors, most notably σ_1 receptors (σ_1Rs) (*12*).

The 3-benzazepine structural class of compounds has recently emerged as potential PET radioligand candidates for the imaging of GluN1/2B (Fig. 1) (*13,14*). Recently, Ametamey's group successfully developed the 3-benzazepin-1-ol derivative, (*R*)-^{11}C-Me-NB1, for imaging GluN1/2B in humans (*15–17*). To overcome the

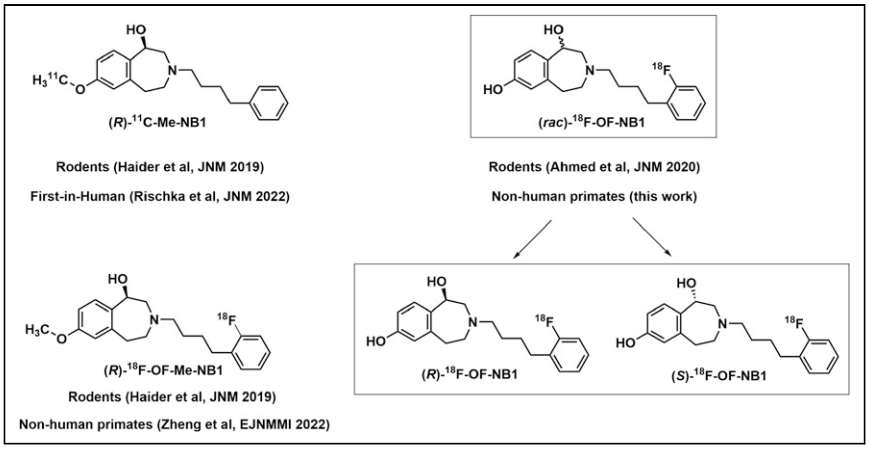

FIGURE 1. Structures of (*R*)-^{11}C-Me-NB1, the lead radiotracer recently evaluated in clinical trial; (*R*)-^{18}F-OF-Me-NB1, the first radiofluorinated derivative of (*R*)-^{11}C-Me-NB1 evaluated in rats; and (*rac*)-, (*R*)-, and (*S*)-^{18}F-OF-NB1 evaluated in the current work.

limitation of the short physical half-life of ^{11}C-labeled radioligands, we evaluated several radiofluorinated derivatives in animals (*18–20*). (*Rac*)-^{18}F-OF-NB1 (inhibition constant K_i (GluN1/2B), 10.4 ± 4.7 nM) emerged as one of the most promising candidates for evaluation in nonhuman primates (*19*). In the current work and for the purpose of clinical translation, we evaluated the pharmacokinetic and imaging properties of (*rac*)-, (*S*)-, and (*R*)-^{18}F-OF-NB1 in nonhuman primates, and performed a comprehensive assessment of (*S*)-^{18}F-OF-NB1 regarding its binding specificity to GluN1/2B receptors and selectivity over σ_1Rs *in vivo*.

MATERIALS AND METHODS

Chemistry

Synthesis of the reference compound (*rac*)-OF-NB1 and the corresponding aryl boronic ester precursors followed previously published procedures, as did their chiral high-performance liquid chromatography (HPLC) separation (*18,19*).

Radiochemistry

^{18}F-fluoride was produced via the ^{18}O(p,n)^{18}F nuclear reaction using $H_2{}^{18}O$ (Huayi Isotopes) in a 16.5-MeV GE Healthcare PETtrace cyclotron. After bombardment, the activity was transferred to a shielded hot cell and trapped on an anionic-exchange resin cartridge (Chromafix PS-HCO_3; Macherey-Nagel). Trapped $^{18}F^-$ was eluted into a sealed 5-mL borosilicate glass reaction vial using a 2-mL solution of $K_2C_2O_4$ (1.0 mg/mL in water), K_2CO_3 (0.1 mg/mL in water), and Kryptofix 222 (Merck) (6.3 mg/mL in acetonitrile). The solution was azeotropically dried for 5 min at 110°C under nitrogen, followed by drying twice using 0.4 mL of acetonitrile each time. Afterward, the vial was purged with 20 mL of air before the addition of 0.4 mL of the boronic ester precursor solution (6 mg of precursor and 12 mg of $Cu(OTf)_2(Py)_4$ in anhydrous dimethylacetamide). The reaction mixture was stirred at 110°C for 20 min, diluted with 10 mL of deionized water, and passed through a Waters C18 SepPak cartridge. The cartridge was washed with 10 mL of deionized water. The trapped activity was eluted from the SepPak with 1 mL of ethanol into a second reaction vial. The solvent was dried at 90°C under a nitrogen stream. Dichloromethane and anhydrous BBr_3 were added and left to react for 15 min at room temperature. The solvent was removed by gentle nitrogen blowing, and the crude product was redissolved in the HPLC mobile phase (25% acetonitrile/75% 0.1 M ammonium formate with 0.5% acetic acid, pH 4.2). The solution was injected into a semipreparative HPLC system equipped with an Agilent Eclipse XDB-C18 (9.4 × 250 mm, 5 μm) column eluting with the above mobile phase at a flow rate of 5 mL/min. The radioactive peak from 15 to 16 min was collected and diluted with 50 mL of water. The solution was passed through a Waters C18 SepPak cartridge. The product was eluted from the SepPak with 1 mL of ethanol and dried under gentle nitrogen blowing. The product was redissolved with the second HPLC mobile phase (32% acetonitrile/68% water with 0.05% triethylamine) and injected into the chiral semipreparative HPLC system equipped with a Regis reflect I-Amylose A column (250 × 10 mm, 5 μm) eluting with the aforementioned mobile phase at a flow rate of 5 mL/min. The radioactive peaks corresponding to (*R*)-^{18}F-OF-NB1 (eluting from 23 to 25 min) and (*S*)-^{18}F-OF-NB1 (eluting from 27 to 29 min) were collected in 2 separate bottles and diluted with 50 mL of water each. The solutions were passed through Waters C18 SepPak cartridges separately. Each SepPak was washed with 1 mM HCl (10 mL), dried with air, and then eluted with 1 mL of U.S. Pharmacopeia–grade ethanol, followed by 3 mL of U.S. Pharmacopeia–grade saline, into a collection vial. The solution was then passed through a 0.22-μm Millex-GV filter (Millipore) into a 10 mL dose vial precharged with 7 mL of U.S. Pharmacopeia–grade saline for formulation.

Measurement of Lipophilicity (log $D_{7.4}$)

The lipophilicity (log $D_{7.4}$) of (*S*)-^{18}F-OF-NB1 was determined according to previously published procedures (*21,22*). The log $D_{7.4}$ was calculated as the ratio between the concentrations of decay-corrected radioactivity in 1-octanol and pH 7.4 phosphate-buffered saline (Dulbecco).

PET Imaging in Rhesus Monkeys

All experimental procedures were approved by the Yale University Institutional Animal Care and Use Committee. In total, 11 dynamic PET scans (120 min each) were performed on 3 rhesus monkeys (*Macaca mulatta,* 2 males and 1 female) on the Focus 220 scanners (Siemens Medical Solutions).

Baseline scans were acquired for (*rac*)-, (*R*)-, and (*S*)-^{18}F-OF-NB1, whereas blockade scans using the GluN1/2B antagonist Co 101244 (0.25 mg/kg; half-maximal inhibition concentration (IC_{50}), 4 ± 1 nM for GluN1/2B) were performed for the enantiopure radiotracers (*23*). Further, blockade scans using either the σ_1R antagonist FTC-146 (2 doses; 0.027 and 0.125 mg/kg; K_i, 0.0025 nM for σ_1R) alone or GluN1/2B (0.25 mg/kg dose of Co 101244) followed by σ_1R blockade (0.125 mg/kg dose of FTC-146) were accomplished using (*S*)-^{18}F-OF-NB1 (*24*). Procedures for PET scanning, image processing, and image analysis are detailed in the supplemental materials (available at http://jnm.snmjournals.org).

Arterial Input Function Measurement and Metabolite Analysis. Plasma activity and parent fraction were determined in accordance with previously published procedures (*25,26*). Radioactivity was measured in whole blood and plasma from arterial samples taken at various time points after radiotracer injection using cross-calibrated γ-counters (Wizard 1480/2480; Perkin Elmer). The radiometabolic profile was investigated by HPLC analysis using a column-switching method with plasma samples from 0, 5, 15, 30, 60, 90, and 120 min after radiotracer injection (*27*). The parent fraction was calculated as the ratio of the radioactivity in parent compound–containing fractions to the total radioactivity measured. Finally, the arterial input function was calculated as the product of total plasma concentrations and the interpolated parent fraction at each time point.

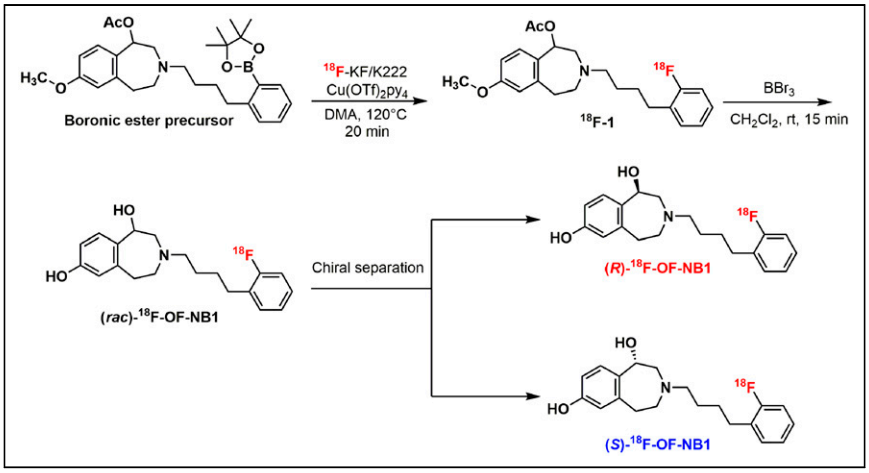

FIGURE 2. Radiosynthesis of (*rac*)-, (*R*)-, and (*S*)-^{18}F-OF-NB1. DMA = dimethylacetamide; rt = room temperature.

Measurement of Radiotracer Free Fraction in Plasma (f_p). Ultrafiltration was the method of choice for measuring the unbound radiotracer in plasma f_p (*28*). The f_p measurement was performed in triplicates per scan and was defined as the ratio of the radioactivity concentration in the filtrate to the total activity in plasma.

Kinetic Modeling. The regional time–activity curves and metabolite-corrected arterial input functions were analyzed with the 1- and 2-tissue compartment models, as well as the multilinear analysis 1 method (starting time, 30 min) to calculate the kinetic parameters (*28*). The regional volume of distribution (V_T, mL/cm^3) from each model was derived and compared. Target occupancy and the nondisplaceable V_T (V_{ND}) in the brain were derived from the Lassen plot, generated using the baseline regional V_T values and the V_T difference between baseline and blockade scans (*29*). Regional binding potential (BP_{ND}) was calculated as $BP_{ND} = (V_T - V_{ND})/V_{ND}$ using the V_{ND} value derived from the Lassen plot for the GluN1/2B blocking scan.

RESULTS

Chemistry

The overall chemical yields of the reference compounds (*rac*)-, (*S*)-, and (*R*)-OF-NB1 and the respective boronic ester precursors were comparable to those published previously (*18,19*).

Radiochemistry

The radiosynthetic strategy is depicted in Figure 2. Despite starting from enantiopure precursors, racemization occurred during the deprotection step, requiring additional chiral purification. The final activities obtained were 1,480 ± 185 MBq (n = 5) for (*rac*)-^{18}F-OF-NB1 and 203.7 ± 81.4 MBq (n = 10) for (*S*)- and (*R*)-^{18}F-OF-NB1. The radiotracers were prepared in more than 99% radiochemical purity. (*S*)- and (*R*)-^{18}F-OF-NB1 were both obtained in more than 98% enantiomeric purity. Molar activity was 143.5 ± 127.3 GBq/μmol (n = 10) at the end of synthesis. The total synthesis time for (*S*)- and (*R*)-^{18}F-OF-NB1 was 200 min on average.

Measurement of log $D_{7.4}$

The measured log $D_{7.4}$ of (*S*)-^{18}F-OF-NB1 was 2.05 ± 0.08 (n = 4), similar to the log $D_{7.4}$ of (*rac*)-^{18}F-OF-NB1, and in the optimal range for brain penetration (*19,30*).

PET Imaging Experiments on Rhesus Monkeys

The amount of injected radioactivity and associated mass were 147.1 ± 47.4 MBq and 1.05 ± 0.70 μg, respectively (n = 10). The parent fractions at 30 min after injection were 33% (n = 2), 32% (n = 2), and 57% (n = 1) for the baseline scans of (*rac*)-, (*S*)-, and (*R*)-^{18}F-OF-NB1, respectively (Fig. 3). For (*S*)- and (*R*)-^{18}F-OF-NB1, the parent fractions decreased to 26% (n = 2) and 27%, respectively, after pretreatment of the animals with the GluN1/2B antagonist Co 101244, whereas preblocking with the σ_1R antagonist FTC-146, whether at a low or a high dose, did not change the parent fraction of (*S*)-^{18}F-OF-NB1 (32%). The f_p was 0.12 ± 0.01 for (*rac*)-^{18}F-OF-NB1 (n = 2), 0.16 ± 0.01 for (*S*)-^{18}F-OF-NB1 (n = 8), and 0.13 for (*R*)-^{18}F-OF-NB1 (n = 1).

In the monkey brain, all tracers showed a heterogeneous distribution, with uptake high in the cortex, putamen, and cerebellum; moderate in the hippocampus and thalamus; and lowest in the centrum semiovale (Fig. 4). Brain uptake of (*S*)-^{18}F-OF-NB1 peaked at an SUV of 4–5 within 20 min after injection, followed by a relatively fast clearance. The (*R*)-enantiomer, on the other hand, displayed slow brain clearance, with uptake increasing throughout the 120-min scan. Brain uptake levels and tissue clearance of (*rac*)-^{18}F-OF-NB1 were between those of the 2 enantiomers (Supplemental Fig. 1). Pretreatment with the GluN1/2B antagonist Co 101244 (0.25 mg/kg) reduced radioactivity levels in all regions to nearly those in the semiovale for both enantiomers at the end of the scans. Receptor occupancy by a 0.25 mg/kg dose of Co 101244 was estimated at 81% and 88% across the brain in 2 separate monkeys for (*S*)-^{18}F-OF-NB1 and 96% for (*R*)-^{18}F-OF-NB1 (Fig. 5). Pretreatment with a σ_1R antagonist reduced the uptake of (*S*)-^{18}F-OF-NB1 across all brain regions. A low dose

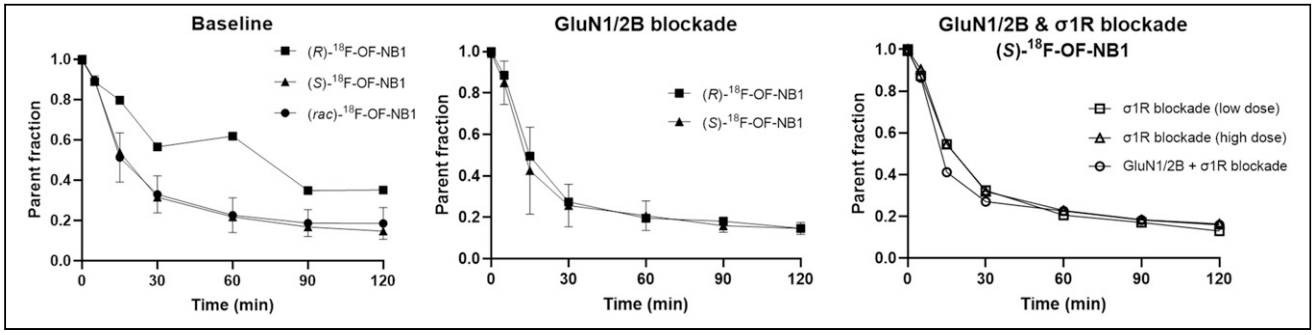

FIGURE 3. Parent fraction remaining of (*rac*)-, (*R*)-, and (*S*)-^{18}F-OF-NB at different time points under baseline and blockade conditions. For GluN1/2B blockade, dose of 0.25 mg/kg of Co 101244 was used. For σ_1R blockade, either low dose (0.027 mg/kg) or high dose (0.125 mg/kg) of FTC-146 was used.

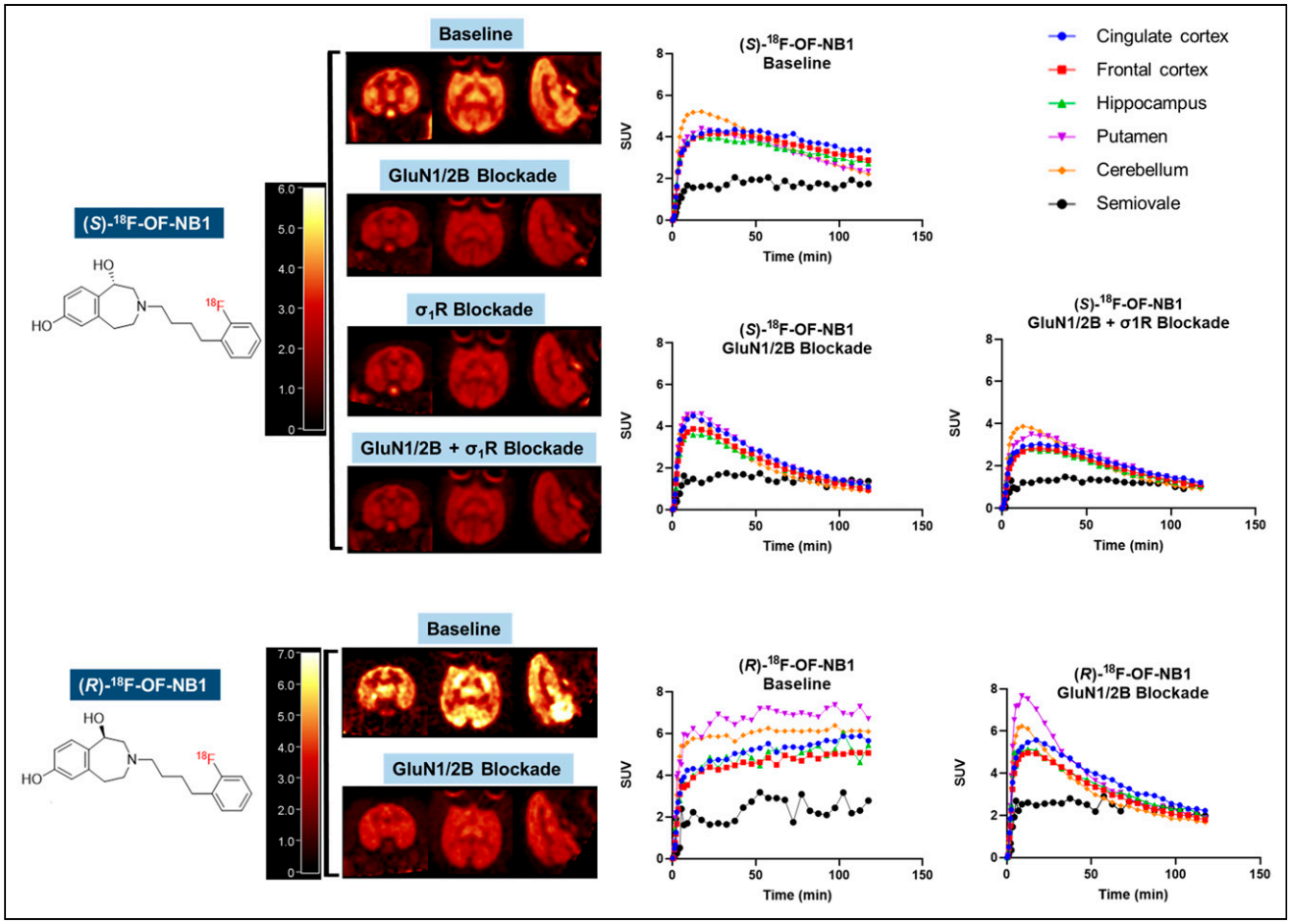

FIGURE 4. (Top) Representative PET SUV images (summed from 45 to 60 min) and time–activity curves in selected brain regions from baseline, GluN1/2B blockade (0.25 mg/kg dose of Co 101244), σ_1R blockade (0.125 mg/kg dose of FTC-146), and sequential GluN1/2B/σ_1R blockade (0.25 mg/kg dose of Co 101244 + 0.125 mg/kg dose FTC-146) scans of (*S*)-^{18}F-OF-NB1 obtained in the same rhesus monkey (monkey 2). (Bottom) PET SUV images and time–activity curves from baseline and GluN1/2B blockade (0.25 mg/kg dose of Co 101244) scans of (*R*)-^{18}F-OF-NB1 (monkey 1).

(0.027 mg/kg) and a high dose (0.125 mg/kg) of FTC-146 reduced the specific binding of (*S*)-^{18}F-OF-NB1 by 48% and 49%, respectively. Double blocking with sequential administration of both Co 101244 (0.25 mg/kg) and high-dose FTC-146 (0.125 mg/kg) in 1 monkey at 25 and 15 min before the radiotracer injection, respectively, did not further reduce brain uptake of (*S*)-^{18}F-OF-NB1 when compared with blocking with Co 101244 alone (82% vs. 81%).

The time–activity curves were well fitted with both the 1-tissue-compartment model and the multilinear analysis 1 method for reliable V_T estimates, with a relative SE of less than 5% (Supplemental Tables 1 and 2). On average, V_T values were similar for (*rac*)- and (*R*)-^{18}F-OF-NB1 and were lower for (*S*)- ^{8}F-OF-NB1. Regional V_T values ranged from 17 to 39 mL/cm^3 for (*S*)-^{18}F-OF-NB1 in the selected brain regions (Table 1). From the GluN1/2B blocking studies, V_{ND} was found to be 9.3 mL/cm^3 for (*S*)-^{18}F-OF-NB1 in monkey 1 and 7.3 mL/cm^3 in monkey 2. From these V_{ND} values, regional BP_{ND} values were calculated and ranged from 1.2 (semiovale) to 3.4 (cingulate cortex) for (*S*)-^{18}F-OF-NB1 (Table 1).

DISCUSSION

Given the involvement of GluN1/2B receptors in various neuropathologies, great effort has been taken to develop therapeutic and PET imaging agents, and several radioligands are currently in development. (*R*)-^{11}C-Me-NB1 was recently evaluated in healthy volunteers and shown to have excellent brain uptake and kinetics (*17*). These results warrant the development of a radiofluorinated PET tracer that would allow wider use. We previously synthesized and tested several ligands, and (*rac*)-^{18}F-OF-NB1 emerged as one of the most promising candidates for clinical translation, given its excellent properties in rodents (*19*). In the current work, we evaluated the performance characteristics of (*rac*)-^{18}F-OF-NB1 and its enantiopure (*S*)- and (*R*)-^{18}F-OF-NB1 with respect to their brain uptake, kinetics, and metabolism, to select the most promising candidate for clinical translation. To our knowledge, there have been no reports of clinical trials on the evaluation of a radiofluorinated probe for PET imaging of GluN1/2B in humans.

The radiosynthesis of ^{18}F-OF-NB1 proceeded in 2 steps: copper-catalyzed radiofluorination of the boronic ester precursor, followed by simultaneous cleavage of the 2 hydroxyl protecting groups (*19*). Despite starting with enantiopure precursors, we could not obtain the respective enantiopure (*S*)- and (*R*)-^{18}F-OF-NB1 without racemization during the second deprotecting step. As such, the radiosynthetic strategy was adapted to include a chiral HPLC purification step to provide enantiopure radiotracers at the end of the synthesis (Supplemental Fig. 2). This allowed the production of both enantiomers from a single radiosynthetic run. Metabolite analysis showed a higher

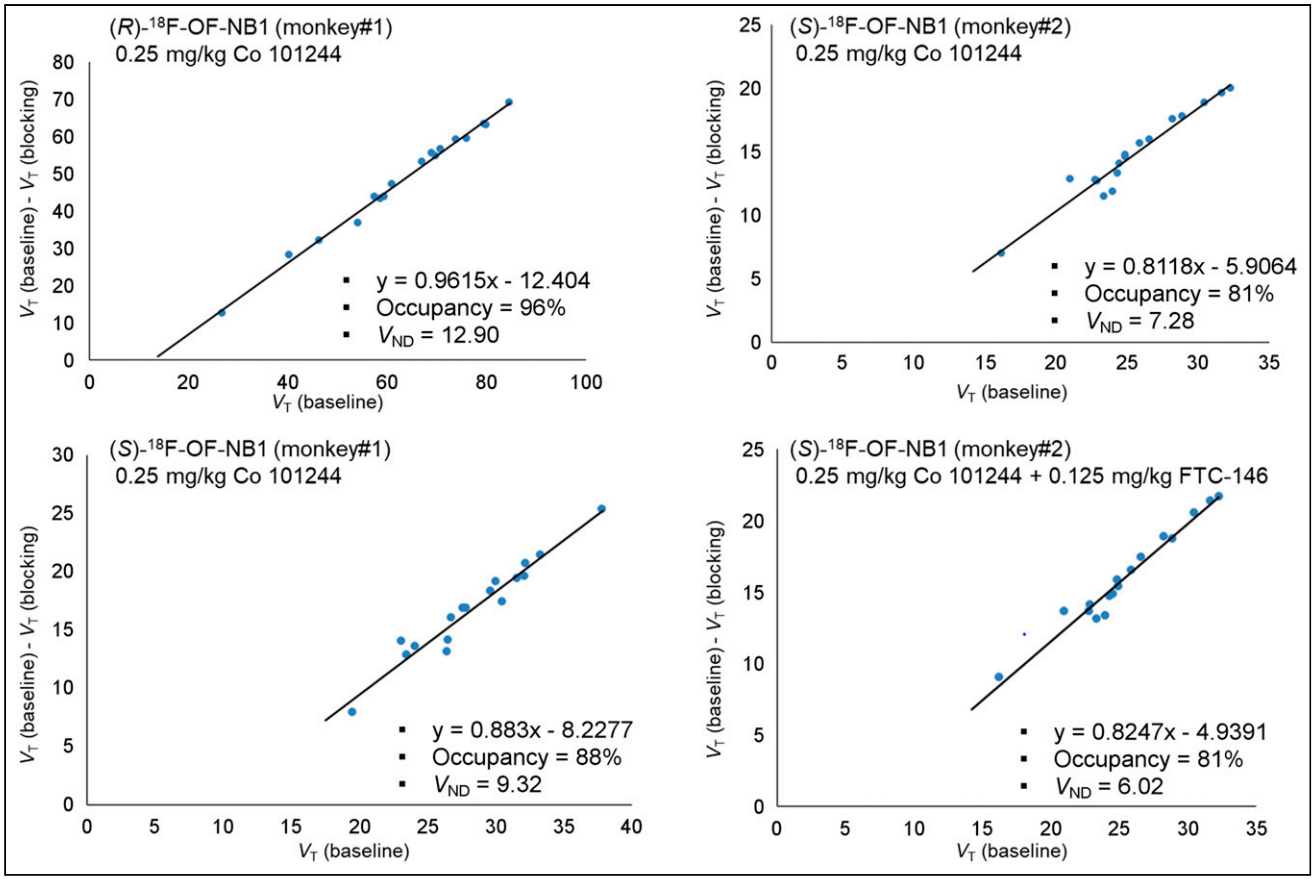

FIGURE 5. Lassen occupancy plots of (*R*)- and (*S*)-^{18}F-OF-NB1 after pretreatment with either GluN1/2B ligand Co 101244 (0.25 mg/kg) only or with addition of σ_1R ligand FTC-146 (0.125 mg/kg). Each point represents unique brain region.

parent fraction in the plasma for (*R*)-^{18}F-OF-NB1 than for the (*S*)-enantiomer. This phenomenon can be explained by the fact that different enantiomers can bind to enzymes with different affinities and therefore exhibit different metabolic rates (*31*). Further, all forms of ^{18}F-OF-NB1 presented good f_p values (0.12–0.16), offering the opportunity for high-precision measurement and subsequently improving the accuracy of quantitative PET measurements and calculation of V_T/f_p, a potentially valuable outcome measure in clinical trials.

The brain uptake and distribution of (*rac*)-^{18}F-OF-NB1 corroborated results in rodents (*19*). Kinetic analysis, however, is not suited for racemic mixtures unless both enantiomers exhibit identical plasma

TABLE 1
One-Tissue-Compartment Model V_T and BP_{ND} Values in Selected Brain Regions Under Baseline and Blockade Conditions

	V_T (mL/cm^3)						BP_{ND}	
	Baseline		Co 101244 (0.25 mg/kg)		FTC-146 (0.027 mg/kg)	FTC-146 (0.125 mg/kg)	$(V_T - V_{ND})/V_{ND}$	
Region of interest	Monkey 1	Monkey 2	Monkey 1	Monkey 2	Monkey 1	Monkey 2	Monkey 1	Monkey 2
Thalamus	24.6 (39.6)	23.3	10.4 (13.7)	10.2	20.9	13.9	1.64 (2.1)	2.20
Cerebellum	27.3 (50.3)	25.5	10.8 (13.1)	10.2	19.6	15.5	1.93 (2.9)	2.50
Cingulate cortex	38.8 (59.5)	32.3	12.6 (16.5)	12.1	27.9	19.3	3.16 (3.6)	3.44
Frontal cortex	31.1 (49.1)	28.9	11.0 (13.8)	10.7	20.9	17.3	2.34 (2.8)	2.97
Hippocampus	32.1 (50.8)	26.3	11.5 (14.6)	10.6	24.0	16.2	2.44 (2.9)	2.61
Semiovale	20.3 (30.9)	16.9	10.6 (13.7)	9.0	15.9	11.5	1.18 (1.4)	1.32

Data in parentheses are for (*R*)-^{18}F-OF-NB1 in 1 monkey; other data are for (*S*)-^{18}F-OF-NB1 in 2 different monkeys. V_{ND} values were derived from GluN1/2B blocking scan using Co 101244.

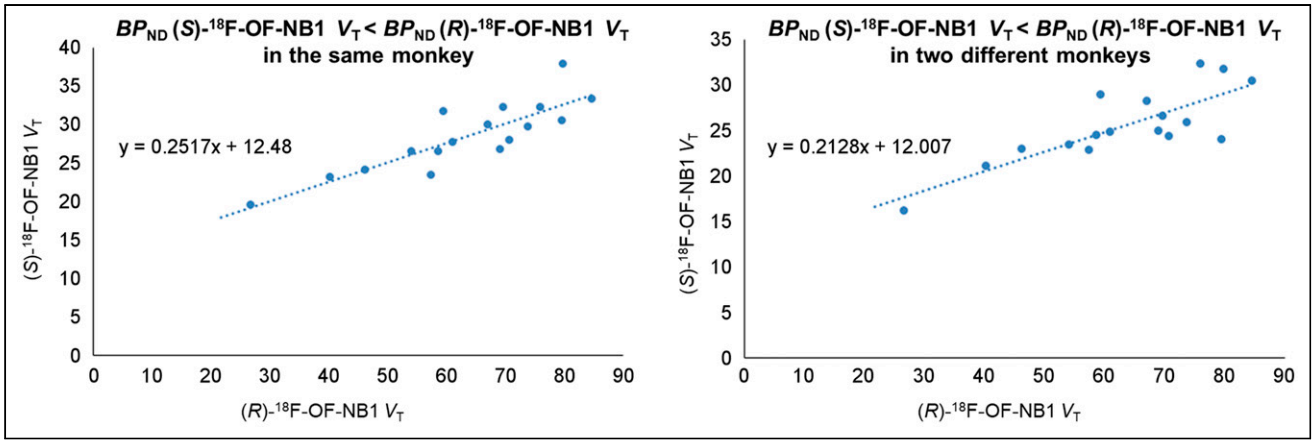

FIGURE 6. Guo plots (*33*) comparing regional V_T values of (*S*)-^{18}F-OF-NB1 (*y*-axis) and (*R*)-^{18}F-OF-NB1 (*x*-axis) in same monkey (left) and in 2 different monkeys (right). *y*-intercept is > 0, signifying higher BP_{ND} values of tracer on *x*-axis than on *y*-axis. Slope indicates relative *in vivo* binding affinity of 2 tracers, where (*R*)-^{18}F-OF-NB1 exhibits 4- to 5-fold higher binding affinity than (*S*)-enantiomer.

clearance. The 2 enantiopure radiotracers displayed brain distribution and kinetics that are in line with the results in rodents. (*R*)- and (*S*)-^{18}F-OF-NB1 showed high uptake in GluN1/2B-rich brain regions, with the highest uptake in the cingulate cortex. The binding of both enantiopure tracers was displaceable across all brain regions, indicating the lack of a reference region for kinetic modeling analysis. Regional time–activity curves of all 3 tracers, on the other hand, were well fitted by the 1-tissue-compartment model. The 2-tissue-compartment model also produced reasonable model fits, but the SE of V_T values was high and nonphysiologic values were generated in several gray matter regions. The multilinear analysis 1 method also provided good fits and V_T values comparable to those derived from the 1-tissue-compartment model (*32*). Regional V_T estimates were higher for (*R*)-^{18}F-OF-NB1 than for the (*S*)-enantiomer. When plotting V_T values of (*R*)- and (*S*)-^{18}F-OF-NB1 against each other to generate the Guo plot (*33*), the slope of this curve indicated 4- to 5-fold higher *in vivo* affinity for (*R*)-^{18}F-OF-NB1 than for (*S*)-^{18}F-OF-NB1 (Fig. 6).

To investigate the *in vivo* binding specificity of both enantiomers to GluN1/2B, blocking experiments with the GluN1/2B antagonist Co 101244 (0.25 mg/kg) were performed and a Lassen plot analysis for each enantiomer was undertaken. Both enantiomers showed high specific binding, with an estimated occupancy of 96% ($n = 1$) across the brain by Co 101244 (0.25 mg/kg) when measured with (*R*)-^{18}F-OF-NB1, and 85% ($n = 2$) with (*S*)-^{18}F-OF-NB1. Furthermore, both enantiomers exhibited good regional BP_{ND} values in the range of 2–3, highlighting their clinical translation potential in terms of specific binding (Table 1). The high affinity of (*R*)-^{18}F-OF-NB1 came at the expense of a less desirable pharmacokinetic profile due to its extremely slow washout from the brain, which precluded its further development, since a very long scan might be required in humans. Pretreatment with a low dose (0.027 mg/kg) or a high dose (0.125 mg/kg) of the σ_1R antagonist FTC-146 led to partial blocking, with a 49% and 48% reduction in the specific binding of (*S*)-^{18}F-OF-NB1, respectively, as calculated from the Lassen plots, and no clear dose–blockade level relationship. To address this potential off-target binding component of (*S*)-^{18}F-OF-NB1, a sequential blockade experiment was conducted in which Co 101244 (0.25 mg/kg) was injected first, followed by the σ_1R antagonist FTC-146 (0.125 mg/kg). Blocking with a 0.25 mg/kg dose of Co 101244 alone resulted in 81% occupancy, and virtually no change in occupancy was observed when FTC-146 was administered afterward. The absence of a further reduction in binding after treatment with FTC-146 suggests that (*S*)-^{18}F-OF-NB1 binds specifically to the GluN1/2B receptors and is selective over σ_1Rs. The partial blockade of (*S*)-^{18}F-OF-NB1 binding by FTC-146 when administered alone can be attributed to σ_1R-NMDAR cross-talk stemming from the inherent chaperone nature of σ_1Rs and their ability to regulate the NMDARs (*34,35*). Another plausible explanation might be off-target binding of FTC-146, as the σ_1R bears a particular binding site that is structurally similar to the ifenprodil-binding site of the GluN1/2B receptor, and thus σ_1R ligands are known for their off-target binding at the GluN1/2B. For example, we have reported potential off-target binding by the σ_1R ligand fluspidine (*19*). Nonetheless, further studies are warranted to clarify the nature of potential off-target binding by these novel benzazepine-based radioligands.

CONCLUSION

We successfully synthesized and evaluated (*rac*)-, (*S*)-, and (*R*)-^{18}F-OF-NB1 in rhesus monkeys. The high GluN1/2B-specific binding of (*S*)-^{18}F-OF-NB1 (gray matter BP_{ND} values in the range of 1.6–3.4) and its attractive pharmacokinetic profile render it a promising candidate for clinical translation. Clinical PET imaging of GluN1/2B could expedite the development of GluN1/2B therapeutics through target engagement and occupancy studies. Furthermore, PET imaging of diseases in which the GluN2B subunit–containing NMDARs are implicated could potentially improve the diagnosis and treatment monitoring of these diseases.

DISCLOSURE

This study was funded by the National Institute of Health (grant U01MH107803) and also was partly supported by the Swiss National Science Foundation (grants 310030E-160403/1 and 310030E-182872/1). Hazem Ahmed, Simon Ametamey, and Ahmed Haider hold shares in Nemosia A.G. No other potential conflict of interest relevant to this article was reported.

ACKNOWLEDGMENTS

We thank the staff at the Yale PET Center for their expert technical support.

KEY POINTS

QUESTION: Can we selectively image GluN2B subunit–containing NMDARs in nonhuman primates and identify a suitable radiofluorinated PET probe for clinical translation?

PERTINENT FINDINGS: (*S*)-^{18}F-OF-NB1 emerged as an attractive candidate for clinical translation, as it displayed high specific binding to GluN1/2B receptors and a favorable pharmacokinetic profile.

IMPLICATIONS FOR PATIENT CARE: A GluN1/2B PET tracer suitable for use in humans will facilitate the investigation and diagnosis of neuropsychiatric diseases, as well as the development of therapeutics targeting GluN2B-containing NMDARs.

REFERENCES

1. Hansen KB, Yi F, Perszyk RE, et al. Structure, function, and allosteric modulation of NMDA receptors. *J Gen Physiol.* 2018;150:1081–1105.
2. Hardingham GE, Bading H. Synaptic versus extrasynaptic NMDA receptor signalling: implications for neurodegenerative disorders. *Nat Rev Neurosci.* 2010;11:682–696.
3. Wang R, Reddy PH. Role of glutamate and NMDA receptors in Alzheimer's disease. *J Alzheimers Dis.* 2017;57:1041–1048.
4. Paoletti P, Bellone C, Zhou Q. NMDA receptor subunit diversity: impact on receptor properties, synaptic plasticity and disease. *Nat Rev Neurosci.* 2013;14:383–400.
5. Adell A. Brain NMDA receptors in schizophrenia and depression. *Biomolecules.* 2020;10:947.
6. Ahmed H, Haider A, Ametamey SM. *N*-methyl-D-aspartate (NMDA) receptor modulators: a patent review (2015-present). *Expert Opin Ther Pat.* 2020;30:743–767.
7. Liu W, Jiang X, Zu Y, et al. A comprehensive description of GluN2B-selective *N*-methyl-D-aspartate (NMDA) receptor antagonists. *Eur J Med Chem.* 2020; 200:112447.
8. Kemp JA, McKernan RM. NMDA receptor pathways as drug targets. *Nat Neurosci.* 2002;5(suppl):1039–1042.
9. Myers SJ, Ruppa KP, Wilson LJ, et al. A glutamate *N*-methyl-D-aspartate (NMDA) receptor subunit 2B-selective inhibitor of NMDA receptor function with enhanced potency at acidic pH and oral bioavailability for clinical use. *J Pharmacol Exp Ther.* 2021;379:41–52.
10. Arakawa R, Takano A, Halldin C. PET technology for drug development in psychiatry. *Neuropsychopharmacol Rep.* 2020;40:114–121.
11. Hargreaves RJ, Rabiner EA. Translational PET imaging research. *Neurobiol Dis.* 2014;61:32–38.
12. Fuchigami T, Nakayama M, Yoshida S. Development of PET and SPECT probes for glutamate receptors. *ScientificWorldJournal.* 2015;2015:716514.
13. Cai L, Liow JS, Morse CL, et al. Evaluation of ^{11}C-NR2B-SMe and its enantiomers as PET radioligands for imaging the NR2B subunit within the NMDA receptor complex in rats. *J Nucl Med.* 2020;61:1212–1220.
14. Krämer SD, Betzel T, Mu L, et al. Evaluation of ^{11}C-Me-NB1 as a potential PET radioligand for measuring GluN2B-containing NMDA receptors, drug occupancy, and receptor cross talk. *J Nucl Med.* 2018;59:698–703.
15. Mu L, Krämer SD, Ahmed H, et al. Neuroimaging with radiopharmaceuticals targeting the glutamatergic system. *Chimia (Aarau).* 2020;74:960–967.
16. Haider A, Herde AM, Krämer SD, et al. Preclinical evaluation of benzazepine-based PET radioligands (*R*)- and (*S*)-^{11}C-Me-NB1 reveals distinct enantiomeric binding patterns and a tightrope walk between GluN2B- and σ_1-receptor-targeted PET imaging. *J Nucl Med.* 2019;60:1167–1173.
17. Rischka L, Vraka C, Pichler V, et al. First-in-humans brain PET imaging of the GluN2B-containing *N*-methyl-D-aspartate receptor with (*R*)-^{11}C-Me-NB1. *J Nucl Med.* 2022;63:936–941.
18. Haider A, Iten I, Ahmed H, et al. Identification and preclinical evaluation of a radiofluorinated benzazepine derivative for imaging the GluN2B subunit of the ionotropic NMDA receptor. *J Nucl Med.* 2018;60:259–266.
19. Ahmed H, Wallimann R, Haider A, et al. Preclinical development of ^{18}F-OF-NB1 for imaging GluN2B-containing *N*-methyl-D-aspartate receptors and its utility as a biomarker for amyotrophic lateral sclerosis. *J Nucl Med.* 2021;62:259–265.
20. Zheng M, Ahmed H, Smart K, et al. Characterization in nonhuman primates of (*R*)-[^{18}F]OF-Me-NB1 and (*S*)-[^{18}F]OF-Me-NB1 for imaging the GluN2B subunits of the NMDA receptor. *Eur J Nucl Med Mol Imaging.* 2022;49:2153–2162.
21. Wilson AA, Jin L, Garcia A, DaSilva JN, Houle S. An admonition when measuring the lipophilicity of radiotracers using counting techniques. *Appl Radiat Isot.* 2001; 54:203–208.
22. Cai Z, Li S, Zhang W, et al. Synthesis and preclinical evaluation of an ^{18}F-labeled synaptic vesicle glycoprotein 2A PET imaging probe: [^{18}F]SynVesT-2. *ACS Chem Neurosci.* 2020;11:592–603.
23. Barta-Szalai G, Borza I, Bozó E, et al. Oxamides as novel NR2B selective NMDA receptor antagonists. *Bioorg Med Chem Lett.* 2004;14:3953–3956.
24. James ML, Shen B, Zavaleta CL, et al. New positron emission tomography (PET) radioligand for imaging σ-1 receptors in living subjects. *J Med Chem.* 2012;55: 8272–8282.
25. Li S, Zheng MQ, Naganawa M, et al. Development and *in vivo* evaluation of a κ-opioid receptor agonist as a PET radiotracer with superior imaging characteristics. *J Nucl Med.* 2019;60:1023–1030.
26. Zheng MQ, Nabulsi N, Kim SJ, et al. Synthesis and evaluation of ^{11}C-LY2795050 as a κ-opioid receptor antagonist radiotracer for PET imaging. *J Nucl Med.* 2013; 54:455–463.
27. Hilton J, Yokoi F, Dannals RF, Ravert HT, Szabo Z, Wong DF. Column-switching HPLC for the analysis of plasma in PET imaging studies. *Nucl Med Biol.* 2000;27: 627–630.
28. Ichise M, Toyama H, Innis RB, Carson RE. Strategies to improve neuroreceptor parameter estimation by linear regression analysis. *J Cereb Blood Flow Metab.* 2002;22:1271–1281.
29. Cunningham VJ, Rabiner EA, Slifstein M, Laruelle M, Gunn RN. Measuring drug occupancy in the absence of a reference region: the Lassen plot re-visited. *J Cereb Blood Flow Metab.* 2010;30:46–50.
30. Pike VW. PET radiotracers: crossing the blood-brain barrier and surviving metabolism. *Trends Pharmacol Sci.* 2009;30:431–440.
31. Shen Z, Lv C, Zeng S. Significance and challenges of stereoselectivity assessing methods in drug metabolism. *J Pharm Anal.* 2016;6:1–10.
32. Smart K, Zheng MQ, Ahmed H, et al. Comparison of three novel radiotracers for GluN2B-containing NMDA receptors in non-human primates: (*R*)-[^{11}C]NR2B-Me, (*R*)-[^{18}F]of-Me-NB1, and (*S*)-[^{18}F]of-NB1. *J Cereb Blood Flow Metab.* 2022; 42:1398–1409.
33. Guo Q, Owen DR, Rabiner EA, Turkheimer FE, Gunn RN. A graphical method to compare the *in vivo* binding potential of PET radioligands in the absence of a reference region: application to [^{11}C]PBR28 and [^{18}F]PBR111 for TSPO imaging. *J Cereb Blood Flow Metab.* 2014;34:1162–1168.
34. Ryskamp DA, Korban S, Zhemkov V, Kraskovskaya N, Bezprozvanny I. Neuronal sigma-1 receptors: signaling functions and protective roles in neurodegenerative diseases. *Front Neurosci.* 2019;13:862.
35. Pabba M, Wong AY, Ahlskog N, et al. NMDA receptors are upregulated and trafficked to the plasma membrane after sigma-1 receptor activation in the rat hippocampus. *J Neurosci.* 2014;34:11325–11338.